ACS OMEGA

http://pubs.acs.org/journal/acsodf

Article

Electric-Field-Induced Phase Change in Copper Oxide Nanostructures

Tina Hesabizadeh,[⊥] Nessrine Jebari,[⊥] Ali Madouri, Géraldine Hallais, Trevor E. Clark, Sanjay K. Behura, Etienne Herth, and Grégory Guisbiers*

Cite This: *ACS Omega* 2021, 6, 33130−33140

Read Online

ACCESS | Metrics & More | Article Recommendations | Supporting Information

ABSTRACT: Transition-metal oxides such as cupric and cuprous oxides are strongly correlated materials made of earth-abundant chemical elements displaying energy band gaps of around 1.2 and 2.1 eV. The ability to design nanostructures of cupric and cuprous oxide semiconductors with in situ phase change and morphological transition will benefit several applications including photovoltaic energy conversion and photoelectrochemical water splitting. Here, we have developed a physicochemical route to synthesize copper oxide nanostructures, enabling the phase change of cupric oxide into cuprous oxide using an electric field of 10^5 V/m in deionized water via a new synthetic design protocol called electric-field-assisted pulsed laser ablation in liquids (EFA-PLAL). The morphology of the nanostructures can also be tuned from a sphere of ∼20 nm to an elongated leaf of ∼3 μm by controlling the intensity of the applied electric field. Futuristically, the materials chemistry occurring during the EFA-PLAL synthesis protocol developed here can be leveraged to design various strongly correlated nanomaterials and heterostructures of other 3d transition-metal oxides.

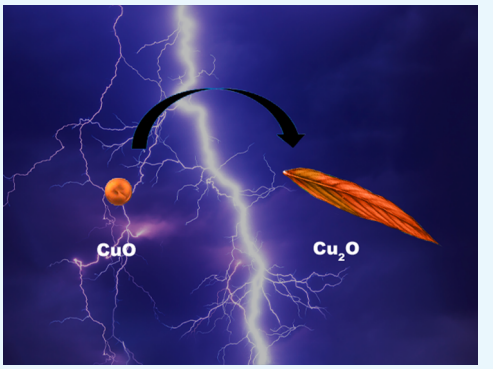

1. INTRODUCTION

Binary oxides of copper such as cupric (CuO) and cuprous (Cu_2O) are p-type semiconducting materials with energy band gaps of ∼1.2 and ∼2.1 eV, respectively.[1] The crystal structure of CuO is monoclinic, which is described by the centrosymmetric space group $C2/c$, whereas Cu_2O has a cubic crystal structure, which belongs to the $pn3$ space group. Within the copper ions, d electrons experience Coulombic repulsion, which tends to localize individual electrons at atomic lattice sites, while hybridization with the oxygen's p electron states tends to delocalize the electrons.[2] These copper oxides (Cu_xO; x = 1 or 2) are consequently materials having the appropriate energy band gap to enable the absorption of light and generate charge carriers via photovoltaic phenomena; and to split the water molecule into hydrogen and oxygen using solar energy through photoelectrochemical phenomena. Indeed, the energy required for water splitting is between 1.6 and 2.4 eV,[3] and Cu_xO has a suitable energy band gap for oxidizing and reducing water. Furthermore, the CuO and Cu_2O nanostructures (NSs) are also used for other applications such as batteries,[4,5] gas sensors,[6] catalysts,[7,8] and pigments.[9]

To further develop several technological applications such as photovoltaic energy conversion and photoelectrochemical water splitting, our ability to design strongly correlated structures of Cu_xO semiconductors with in situ phase change and morphological transition is crucial. There exist several thermodynamic pathways to promote the phase change of CuO into Cu_2O.[10] Recently, some studies have reported the synthesis of Cu_xO NSs by the hydrothermal method[11] and CuO nanowires (NWs) by an electric-field-assisted thermal oxidation method.[12] Electric field plays a critical role in controlling the growth and morphology of the synthesized CuO NWs as ion diffusion and velocity can be tuned via an external electric field.[12] Earlier studies had also investigated the role of electrical discharges with various conductivities (chemically controlled) on the growth of Cu-based NSs.[13]

We present here a new pathway to induce a phase transition in Cu_xO NSs by transforming CuO into Cu_2O using an electric field, which is mechanistically understood via the Oswald ripening process. Indeed, by increasing the value of the electric field from 0 to 10^5 V/m, there is a structural phase change from CuO to Cu_2O. Moreover, there is also a morphological transition, accompanying the structural change, evolving from a sphere of ∼20 nm to an elongated leaf of ∼3 μm. This paper reports for the very first time a synthesis of Cu_xO NSs by electric-field-assisted-pulsed laser ablation in liquids (EFA-PLAL).

Received: October 3, 2021
Accepted: November 4, 2021
Published: November 22, 2021

https://doi.org/10.1021/acsomega.1c05498
ACS Omega 2021, 6, 33130−33140

Table 1. Cu_xO NSs Synthesized by Laser Ablation in Liquids (LAL)[a]

ref	type of laser	repetition rate (Hz)	irradiation time (min)	solvent	energy/pulse or fluence	result
Femtosecond − PLAL						
14	Ti:Sapphire at 800 nm	1000	9	deionized (DI) water, acetone	500 μJ/pulse and 50 μJ/pulse	Cu at Cu_2O NPs and Cu_2O at Cu NPs
Picosecond − PLAL						
15	Nd:YAG at 532 nm	10	60	DI water, ethanol	31 mJ/pulse	Cu_2O NPs
Nanosecond − PLAL						
16	Nd:YAG at 355 nm	10	60	DI water	150 mJ/pulse	Cu/CuO NPs
17	Nd:YAG at 532 nm	10	15, 30	spinach water extract	200 mJ/pulse	
18	Nd:YAG at 532 nm			DI water	20 mJ/pulse	CuO NPs
19	Nd:YAG at 532 nm	6	15, 30, 45, 60	DI water	30 mJ/pulse	CuO NPs
20	Nd:YAG at 532 nm	10	15	DI water with hydrogen peroxide (0−5%)	60 mJ/pulse	CuO and Cu_2O NPs
21	Nd:YAG at 532 nm	10		DI water	25 mJ/pulse	Cu a tCu_2O NPs
22	Nd:YAG at 1064 nm	1	5−20	DI water	40−200 mJ/pulse	CuO NPs
23	Nd:YAG at 1064 nm		10	DI water, acetonitrile, methanol, ethanol, hexane, 1-propanol, butanol, ethylene glycol	80 mJ/pulse	
24	Nd:YAG at 1064 nm	10		poly(vinyl alcohol)	75 mJ/pulse	
25	Nd:YAG at 1064 nm	10	60	DI water, ethylene glycol	27 J/cm^2 and 80 J/cm^2	hollow CuO NPs and Cu NPs
26	Nd:YAG at 1064 nm	10	4	ethanol	1.5 J/pulse	Cu_2O NPs
27	Nd:YAG at 1064 nm			DI water	40 mJ/pulse	CuO and Cu_2O NPs
28	Nd:YAG at 1064 nm	20		DI water, sodium hydroxide, hydrogen peroxide, ethyl alcohol		
29	Nd:YAG at 532 nm	10	15, 30, 60	methanol, 2-propanol	30 mJ/pulse	Cu at Cu_2O NPs
30	Nd:YAG at 1064 nm	10	60	PVP aqueous solution	80 mJ/pulse	Cu_2O at CuO NPs
31	Nd:YAG at 1064 nm	10	5	DI water, acetone	130 mJ/pulse	CuO NPs, Cu NPs
32	Nd:YAG at 1064 nm	10	1.66	DI water	10 mJ/pulse	Cu/CuO NPs
33	Nd:YAG at 1064 nm	20	60	DI water	180 mJ/pulse	Cu_2O NPs
34	Ce:Nd:YAG at 1064 nm	10	30	hydrogen peroxide	40, 70, 100 mJ/pulse	Cu/CuO flakes
35	Yb fiber at 1064 nm	21 000		DI water	1 mJ/pulse	CuO NPs
Continuous − LAL						
32	diode laser at 530 nm	CW	120	DI water	/	Cu/CuO NPs
Nanosecond − EFA-PLAL						
this work	**Nd:YAG at 1064 nm**	**1000−15 000**	**30 + 30**	**DI water**	**350 J/cm^2**	**CuO/Cu_2O NSs**

[a]LAL, laser ablation in liquids; PLAL, pulsed laser ablation in liquids; EFA-PLAL, electric-field-assisted-PLAL.

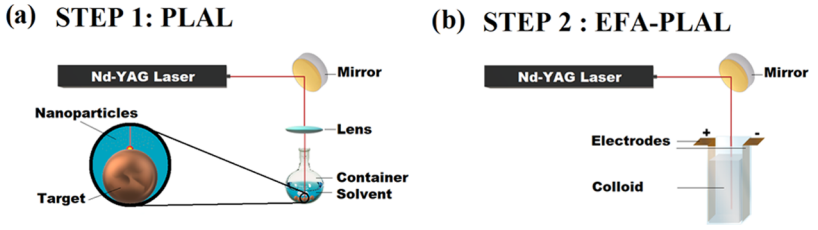

Figure 1. (a, b) Sketch of the synthesis protocol. Step 1 uses a PLAL setup, while step 2 uses an EFA-PLAL setup.

https://doi.org/10.1021/acsomega.1c05498
ACS Omega 2021, 6, 33130−33140

2. EFA-PLAL SYNTHESIS, MECHANISM, AND CHARACTERIZATION

2.1. Background. Cu_xO nanostructures (NSs) can be obtained by various methods including the hydrothermal synthetic method, chemical precipitation methods, thermal conversion of precursors, electrochemical method, thermal oxidation method, and pulsed laser ablation in liquids (PLAL).[1] PLAL is an interesting technique as it produces NSs with a naked surface. A complete list of Cu_xO NSs performed by PLAL is given in Table 1.

2.2. Synthesis. The NSs were created using a two-step process. The first step was a regular PLAL setup (Figure 1a). A Q-switched Nd:YAG laser from Electro Scientific Industries operating at 1064 nm was used to irradiate a Cu target. Spherical Cu beads (99.99% from Sigma Aldrich) were used as targets in this experiment. The diameter of the beads was ∼2 mm. A 25 mL rounded flask was used as a container, and 3 mL of DI water was poured into it. Consequently, the height of the liquid above the surface of the target was measured to be 10 mm. The pulse repetition rate of the laser was varied from 1 to 15 kHz. Consequently, the pulse duration time varied slightly from 70 to 200 ns depending on the repetition rate. The laser shined a pulsed beam with an energy per pulse of around 5.5 mJ per pulse at 1 kHz. The beam was deflected by a flat mirror oriented at a 45° angle (with respect to the laser rail) to irradiate the target from the top and was then focused using an 83 mm focal length lens. The beam's spot size on the target was measured by scanning electron microscopy (SEM) to be around ∼45 μm. Therefore, the intensity of the laser was determined to be around $\sim 3.5 \times 10^5$ W/cm^2. At 1 kHz, the fluence was calculated to be $\sim 3.5 \times 10^2$ J/cm^2. The Cu target was finally irradiated for 30 min.

The second step is an EFA-PLAL setup, as depicted in Figure 1b. EFA-PLAL differs from the PLAL setup in using a direct-current (DC) electric field with adjustable voltage from two parallel electrodes being applied on both sides of the Cu target.[36] The electrodes were two rectangular plates made of Cu. The laser beam was unfocused during the second step, and the target was removed from the container. The colloid obtained after the first step was irradiated for another 30 min. The container was a square cuvette with the electrodes placed face to face on two opposite walls of the cuvette. The potential difference applied between the electrodes was kept constant during the entire duration of the second step at 0, 100, 250, 500, 750, or 1000 V. All of the synthesis details are summarized in Table 2.

Table 2. Parameters of the EFA-PLAL Synthesis

parameter	step 1	step 2
mode	PLAL	EFA-PLAL
laser	Nd:YAG	Nd:YAG
wavelength (nm)	1064	1064
repetition rate (kHz)	5.1	5.1
duration (min)	30	30
target	Cu beads	_
beam	focused	unfocused
volume (mL)	3	3
container	25 mL single-neck rounded flask	3 mL square cuvette

2.3. Mechanism. The solvent used in this synthesis protocol, DI water in our case, confines the plasma plume and also provides a reactive medium to generate a compound based on the target's chemical element, in this case, Cu. The electron configuration of Cu is $[Ar]3d^{10}4s^1$, meaning that Cu has 11 valence electrons, 1 belonging to the 4s orbital and 10 belonging to the 3d orbital.[37] When the laser beam hits the Cu target, it starts ionizing Cu into Cu^+ and $1e^-$, by removing the electron from the 4s orbital. Another electron can easily be removed from the 3d orbital to form Cu^{++}. The laser beam also break downs the water molecule of the solvent into hydrogen ions (H^+) and oxygen ions (O^{2-}) or into hydrogen ions and hydroxide groups (OH^-). When the plasma cools down (laser beam is off), the Cu^+ ions, Cu^{++} ions, H^+ ions, O^{2-} ions, and electrons (e^-) start reacting all together to form CuO or Cu_2O according to the chemical reactions shown in Scheme 1.

Based on the ionic species present during the irradiation, Cu^+ ions and Cu^{++} ions will react with O^{2-} because the enthalpy of formation of Cu_xO is more negative than the enthalpy of formation of copper hydrides (CuH or CuH_2). Moreover, the chemical reaction among Cu^{2+}, OH^-, and e^- will not occur under our synthesis conditions despite a favorable formation enthalpy. Indeed, the presence of the electric field influences the way Cu will be ionized. Without an electric field being present, Cu can be ionized two times into Cu^{++} as the Cu^+ ions do not move (no electric field present) after being ionized the first time by the laser beam. Therefore, CuO is expected without an electric field. When an electric field is present, the Cu^+ ions created by the interaction of the laser beam and the Cu target move along the electric field lines and consequently leave the ablation area; therefore, Cu^+ ions cannot be reirradiated a second time by the laser beam to form Cu^{++}. Thus, Cu_2O is expected when an electric field is present.

2.4. Characterization. The colloids were then characterized by atomic emission spectroscopy (4210 MP-AES from Agilent), scanning electron microscopy (JEOL JSM-7000F, equipped with a field emission gun, and operating at 15 kV), and transmission electron microscopy (Thermo Fisher Scientific Talos F200X operating at 200 kV). To perform Raman, FT-IR, and SEM analyses, a droplet of colloids was deposited onto a silicon wafer and dried in an environmentally controlled glovebox. The samples for the TEM study were each prepared by the drop-casting of one droplet of the colloid onto a TEM grid followed by air-drying. Raman spectra were obtained with a RENISHAW inVia Qontor confocal Raman microscope with thermoelectric cooling for ultralow noise levels. The spectra were recorded in a backscattering configuration with ultrafast data collection (over 1800 spectra per second). The excitation line was at 532 nm, and the laser power was kept at 50% of the source power to avoid heating the samples. The IR measurements were performed using a Varian 670 FT-IR spectrometer.

3. RESULTS AND DISCUSSION

The lifetime of the cavitation bubble can be determined by analyzing the concentration of the colloid versus the repetition rate of the laser (Figure 2a). At low repetition rates, the concentration of NSs increases with the repetition rate. However, by shining the laser beam too fast on the target, the laser will encounter the cavitation bubble, which will correspond to a decrease in concentration of NSs within the colloid. From Figure 2a, it is seen that the maximal production of NSs is reached at 5.1 ± 0.1 kHz; consequently, the

https://doi.org/10.1021/acsomega.1c05498
ACS Omega 2021, 6, 33130−33140

Scheme 1. Possible Chemical Reactions Occurring during the EFA-PLAL Synthesis Protocol

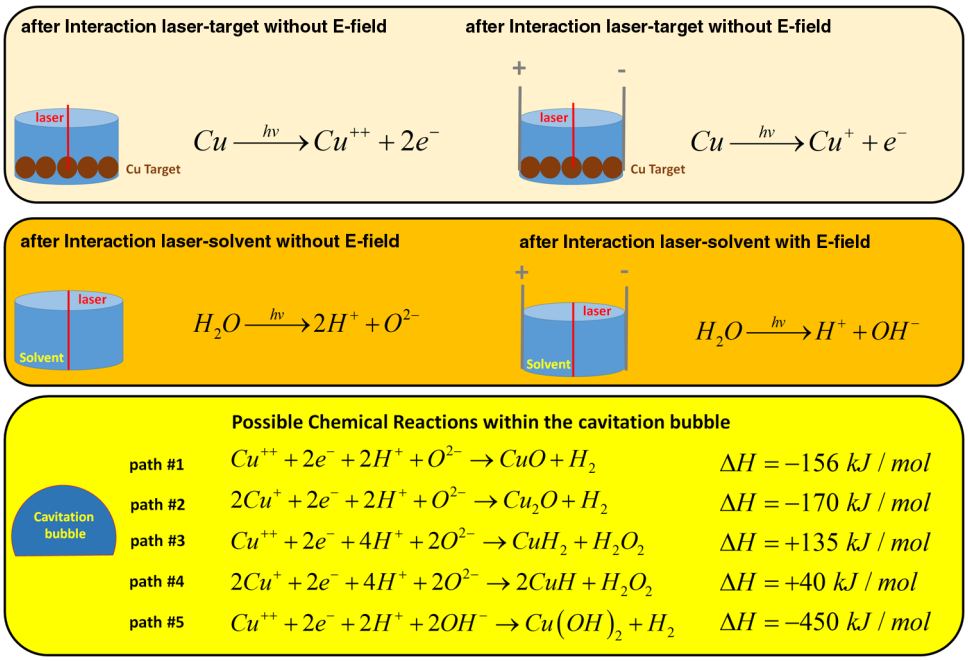

cavitation bubble lifetime is estimated to be ~0.196 ± 0.004 ms. At 10.2 kHz, there is a second peak that still produces some significant amount of NSs, but the concentration is less than the one at 5.1 kHz because approximately only half of the laser shoots reach the target.

After determining the best repetition (5.1 kHz) to irradiate the Cu target in DI water, the electric field was activated during the synthesis to generate five colloids at various voltages of 100, 250, 500, 750, and 1000 V. Another sample (at 0 V) was synthesized without the electric field to serve as a reference. A picture of the sample's series can be seen in the inset in Figure 2b. Figure 2b shows the concentration of Cu-based NSs within each of the colloids synthesized at various voltages. As seen in Figure 2b, the concentration is multiplied by ~5 in comparison to the colloid synthesized without any applied voltage. This can be understood by having the electric field ON between the electrodes; the cavitation bubble is shifted spatially, allowing the laser to reach the target without encountering any shielding effect due to the cavitation bubble and, consequently, enhancing the ablation of Cu. Consequently, the colloids (0, 100, 250, 500, 750, and 1000 V) are acidic by exhibiting a pH around ~6.7 (Figure 2c). Indeed, the presence of Cu_xO nanoparticles (NPs) in the solvent decreases the pH of the solvent compared to a pure DI water solvent, whatever the synthesis protocol is, PLAL or EFA-PLAL. In the Supporting Information, the pH of the colloid is also plotted as a function of the concentration of Cu_xO NSs within the colloid (Figure S1). From Figure S1, it is clear that the EFA-PLAL was very efficient to increase the concentration of NSs with respect to a regular PLAL protocol. In Figure 2d, the temperature of the colloid was monitored, and its value increased with the value of the electric field applied during the synthesis.

The presence of two phases of Cu_xO was detected by Raman spectroscopy (Figure 3a). Indeed, in Figure 3a, each colloid displays some peaks belonging to both oxides CuO and Cu_2O. However, it seems that by increasing the value of the electric field during the synthesis, Cu_2O is promoted compared to CuO. CuO seems to dominate the colloid at a low electric field. At 0 V, the oxidation state of Cu is II, consequently forming CuO NSs. By increasing the potential difference during the synthesis, the oxidation state of Cu decreases to I and forms Cu_2O NSs. The Raman peaks of CuO and Cu_2O are listed in Table 3. In the A_g and B_g Raman modes, only the oxygen atoms move, with displacements in the *b*-direction for A_g and perpendicular to the *b*-axis for B_g modes. The presence of CuO and Cu_2O was also confirmed by FT-IR (Figure 3b). The infrared active modes involve the motion of both O and the Cu atoms. The vibration modes of CuO and Cu_2O are illustrated in Figure 3c. The presence of IR bands at 900, 1100, and 2950 cm^{-1} confirm the Cu_2O phase, while the presence of bands at 600, 750, and 2350 cm^{-1} affirm the CuO phase.

The nature of the oxide present at the surface of the nanostructure has been investigated by X-ray photoelectron spectroscopy (XPS). The PLAL sample synthesized at 0 V looks very different from all of the other samples synthesized with a nonzero potential difference (EFA-PLAL), as can be seen in Figure 4. It is possible to distinguish the Cu oxidation states using the satellite peak features of Cu 2p.[43,44] In Figure 4a, there is a weak satellite peak around ~944 eV, indicating the presence of Cu_2O at the surface. In Figure 4b–f, there are two strong satellite peaks around ~945 and ~965 eV, indicating the presence of CuO at the surface of the NSs.

Finally, the morphology of Cu_xO NSs was analyzed by SEM and is shown in Figure 5. At 0 V, the Cu_xO NSs are spherical; however, at nonzero voltages, the NSs are elongated into leaves. The larger size of NSs obtained at higher potential differences can be explained by the larger temperatures reached by the colloid during the synthesis when the electric field is applied (Figure 2d). Indeed, the more intense the electric field (i.e., potential difference across the cuvette), the higher the temperature. Consequently, the NSs become bigger because of the Oswald ripening process.[45] This process is a heat-induced size change of NSs in solution. By increasing the potential difference from 0 to 1000 V, the surface-to-volume ratio of the NSs increases by having the morphology evolving from a sphere to a nanoleaf. Furthermore, the composition of Cu_xO

https://doi.org/10.1021/acsomega.1c05498
ACS Omega 2021, 6, 33130−33140

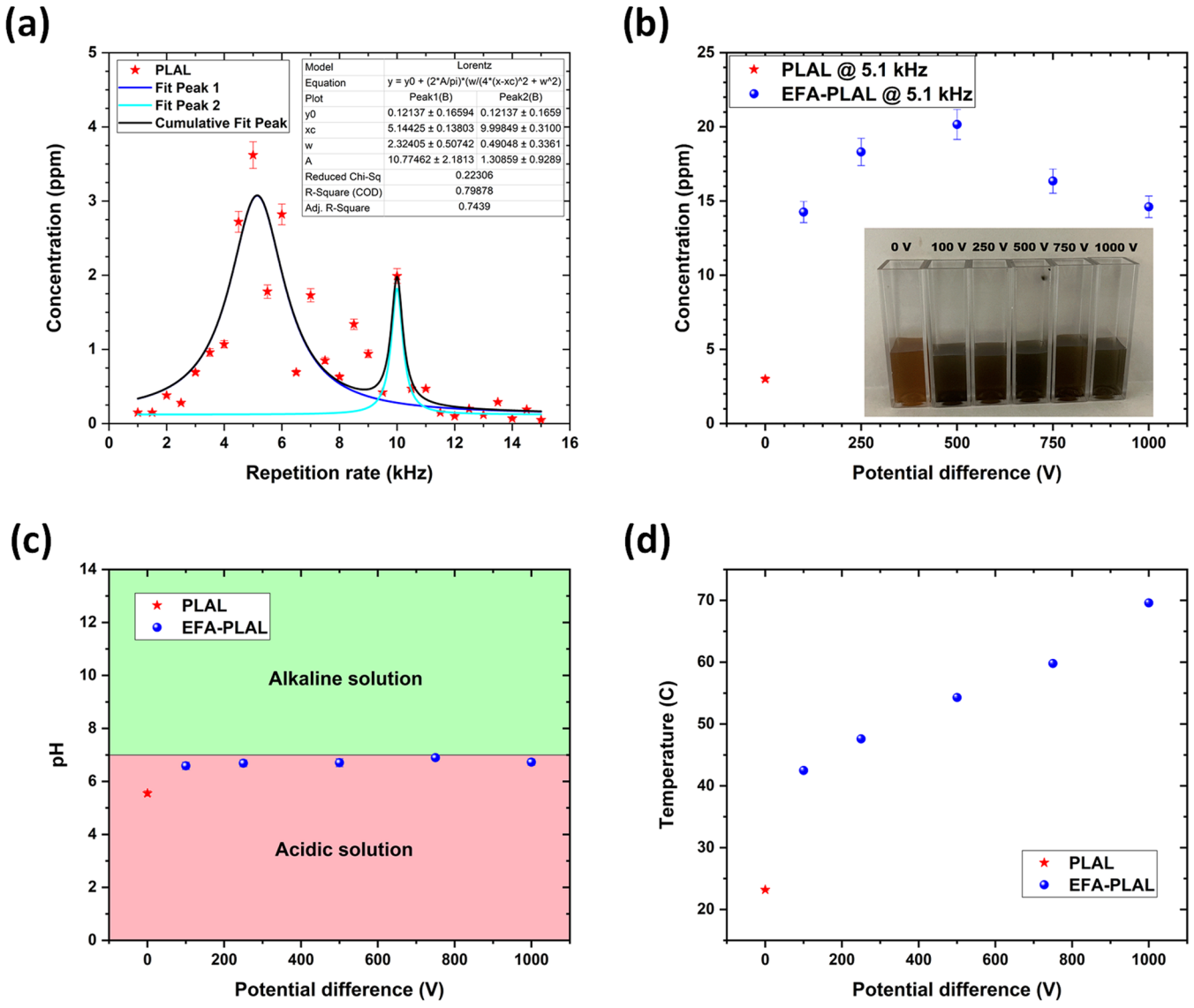

Figure 2. (a) Concentration of Cu_xO colloids synthesized at 0 V for various repetition rates from 1 kHz up to 15 kHz. The optimal repetition rate was determined at ∼5.1 kHz. (b) Concentration of Cu_xO colloids synthesized at 5.1 kHz for various potential differences from 0 V up to 1000 V. Inset: Photo of the colloids synthesized at 5.1 kHz under various potential differences. (c) pH of the Cu_xO colloids synthesized at 5.1 kHz versus the potential difference used during the synthesis. All of the pH values have been measured at room temperature ($T \sim 23$ °C). (d) Temperature of the colloids synthesized at 5.1 kHz versus the potential difference used during the synthesis.

seems also to evolve from CuO to Cu_2O when the potential difference increases from 0 to 1000 V (Figure 3a). This effect on the chemical composition may also be explained by the Oswald ripening process.[46] However, the Oswald ripening process explains why we observe larger structures at higher potential differences but does not explain the elongation. Indeed, the elongation is due to a growth-oriented attachment process occurring by aligning the seeds along the direction of the electric field, consequently creating nanoleaves when an electric field is applied. More SEM images are shown in Figure S2.

In Figure 6, let us focus on the synthesized NSs synthesized under the two most extreme potential differences, i.e., 0 V and 1000. The sample at 0 V shows CuO NPs with sizes smaller than 20 nm, while the sample at 1000 V shows Cu_2O NSs with the length reaching several hundreds of nanometers (inset). It is still possible to encounter spherical NPs in the sample at 1000 V as the spherical NPs produced during the first step process may not have crossed the laser beam path during the second step process. The electron diffraction of both samples confirms the crystallinity of the NSs produced.

The Tauc plot calculated from the absorbance curve obtained by UV−visible spectroscopy on these two extreme samples shows energy band gaps around 2.6 and 3.2 eV at 0 and 1000 V, respectively. Based on the previous discussion, it is evident that the CuO NSs displayed a band gap around 2.6 eV, while Cu_2O NSs exhibited a band gap around 3.2 eV. This is in good agreement with what is observed in the literature.[47,48] These values are much larger than the bulk energy band gaps of CuO and Cu_2O (1.2 and 2.1 eV, respectively). This is due to the small size of the Cu_xO NSs, as shown in Figure 7. Indeed, as the size decreases, the energy band gap increases.[49,50]

To further confirm the electric-field-induced phase transition in the synthesized Cu_xO NSs, we performed TEM and selected area electron diffraction (SAED) studies. The typical diameter of CuO nanoparticles prepared at 0 V is observed to be ∼20

https://doi.org/10.1021/acsomega.1c05498
ACS Omega 2021, 6, 33130−33140

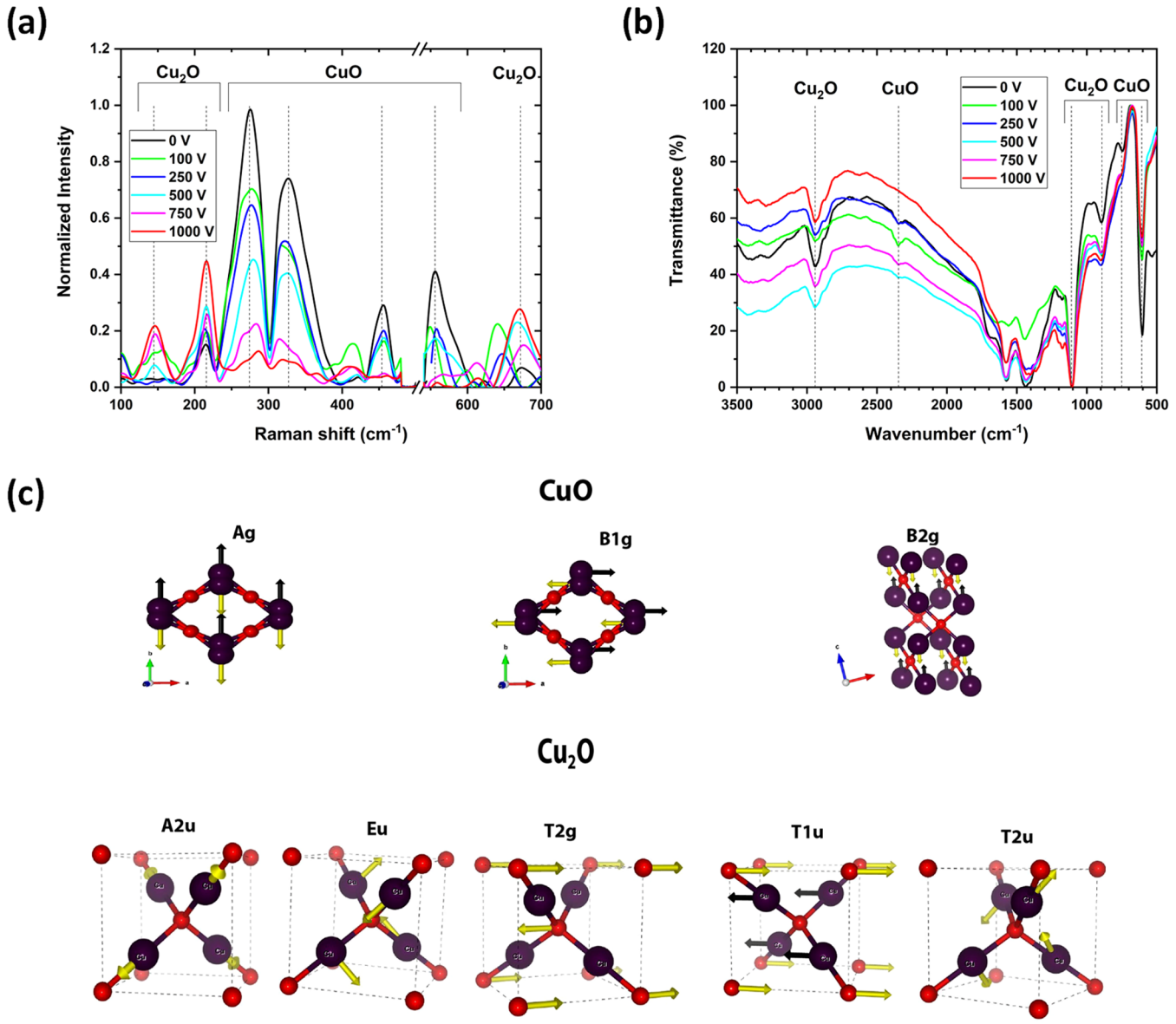

Figure 3. (a) Raman spectra of the colloids synthesized at 5.1 kHz under various potential differences. (b) FT-IR spectra of the colloids synthesized at 5.1 kHz under various potential differences. (c) Illustration showing the vibrational modes for CuO and Cu_2O.

Table 3. Theoretical and Experimental Raman Frequencies of CuO and Cu_2O

material	vibrational mode	theoretical (cm^{-1})	experimental[a] (cm^{-1})
CuO	A_g	294,[38] 296,[39] 298,[40] 319[41]	276
	B_g	348,[38] 346,[39] 345,[40] 382[41]	327
	A_u	421[38]	455
	B_g	624,[38] 631,[39] 632,[40] 639[41]	671
Cu_2O	T_{2u}/Γ25-	88[42]	not observed
	E_u/Γ12-	110[42]	145
	T_{1u}/Γ15-	149,[42] 153[42]	216
	A_{2u}/Γ2-	348[42]	not observed
	T_{2g}/Γ25+	515[42]	not observed
	T_{1u}/Γ15-	640,[42] 660[42]	672

[a]This work.

nm, which is shown in Figure 7a. The corresponding SAED pattern (Figure 7c) confirms the presence of the CuO phase with (022), (−202), and (002) crystal planes with concentric rings of distinct bright spots confirming the crystalline structure of CuO NSs. In contrast, the TEM topography image (Figure 7b) for the samples prepared at 1000 V shows elongated leaflike NSs of over 250 nm. The corresponding SAED pattern in Figure 7d demonstrates the presence of several crystal planes such as (331), (311), (022), (111), (−202), and (002), confirming the formation of both CuO and Cu_2O crystalline phases.

5. CONCLUSIONS

Cu_xO NSs have been successfully synthesized by the EFA-PLAL technique. The first step of the synthesis protocol serves to synthesize the Cu_xO seeds, while the second step serves to elongate the seeds into their final shape. The intensity of the electric field has a huge influence on the morphology of the NSs and the crystalline phase of the oxide formed. When the electric field is OFF, the NSs are spherical, while when the electric field is ON, elongated nanoleaves are formed. The electric field used during the synthesis also helps control the

https://doi.org/10.1021/acsomega.1c05498
ACS Omega 2021, 6, 33130−33140

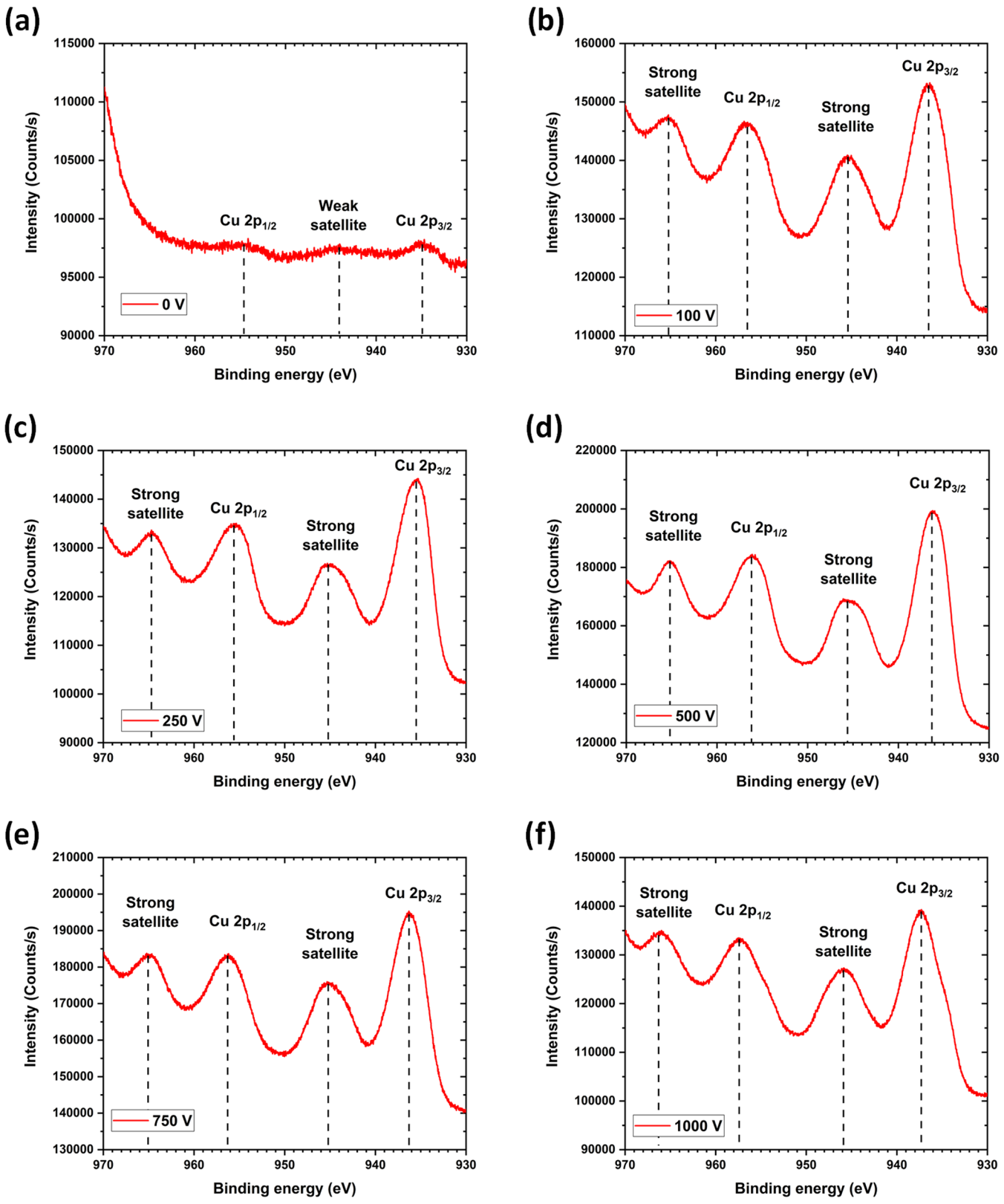

Figure 4. XPS of the Cu_xO NSs synthesized at 5.1 kHz under various potential differences: (a) 0 V, (b) 100 V, (c) 250 V, (d) 500 V, (e) 750 V, and (f) 1000 V.

oxidation state of Cu by promoting a phase transition from CuO to Cu_2O. At low electric fields, Cu II (CuO) is favored, while at higher electric fields, Cu I (Cu_2O) is preferred. Indeed, from the Raman and XPS analyses, it is clear that at 0 V the core and the surface of the spherical nanoparticles are made of CuO, while at 1000 V, Cu_2O becomes predominant in the core and the surface. Also, the two structures displayed significantly different energy band gaps around 2.6 eV for the

https://doi.org/10.1021/acsomega.1c05498
ACS Omega 2021, 6, 33130−33140

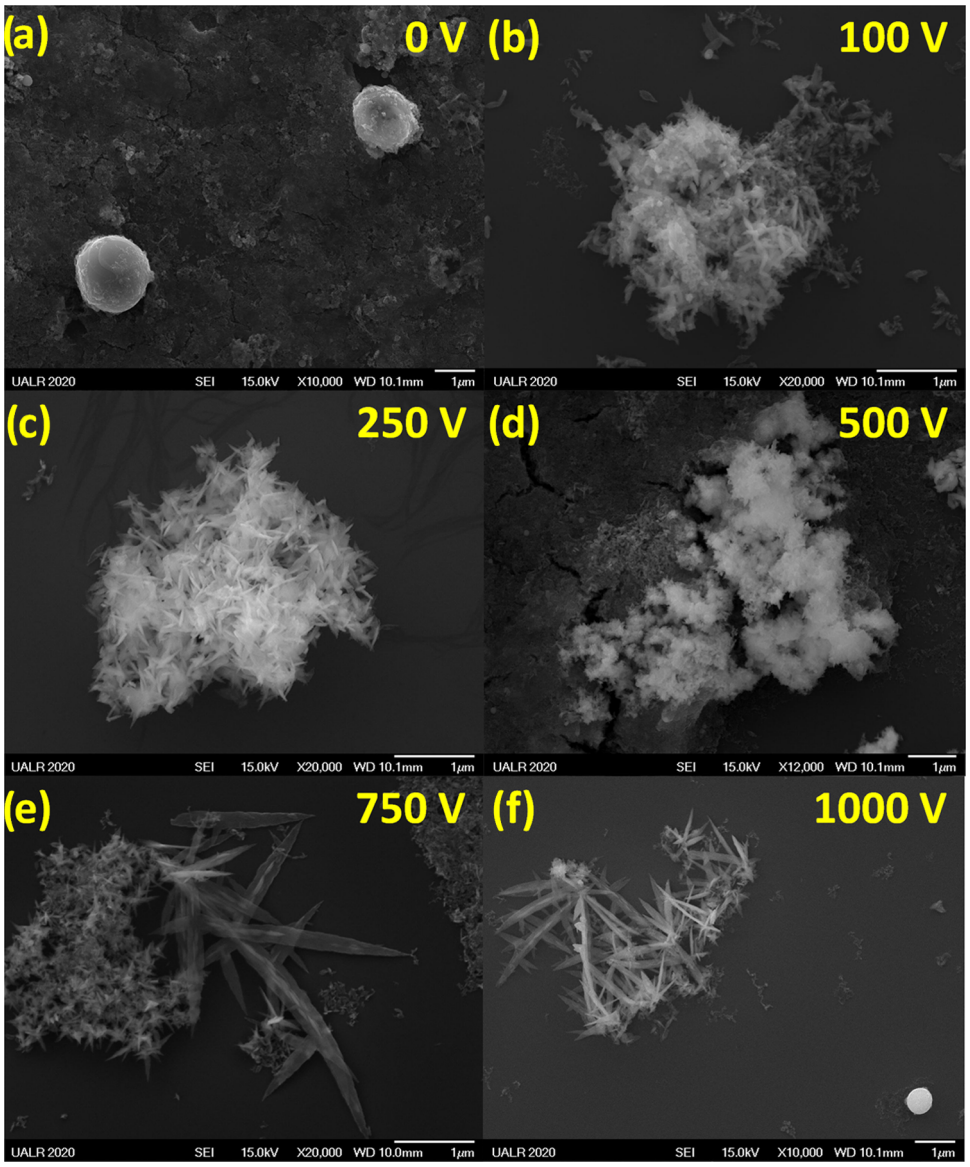

Figure 5. SEM images of the Cu_xO NSs synthesized at 5.1 kHz under various potential differences: (a) 0 V, (b) 100 V, (c) 250 V, (d) 500 V, (e) 750 V, and (f) 1000 V.

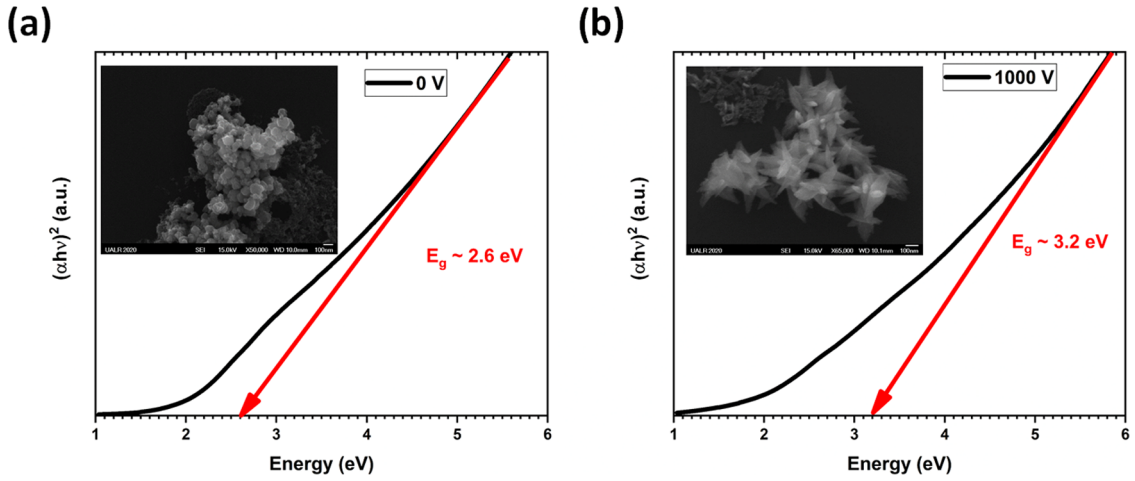

Figure 6. (a, b) Tauc plots of the Cu_xO NSs synthesized at 5.1 kHz under potential differences of 0 and 1000 V, respectively. Inset: SEM image of the Cu_xO NSs.

https://doi.org/10.1021/acsomega.1c05498
ACS Omega 2021, 6, 33130−33140

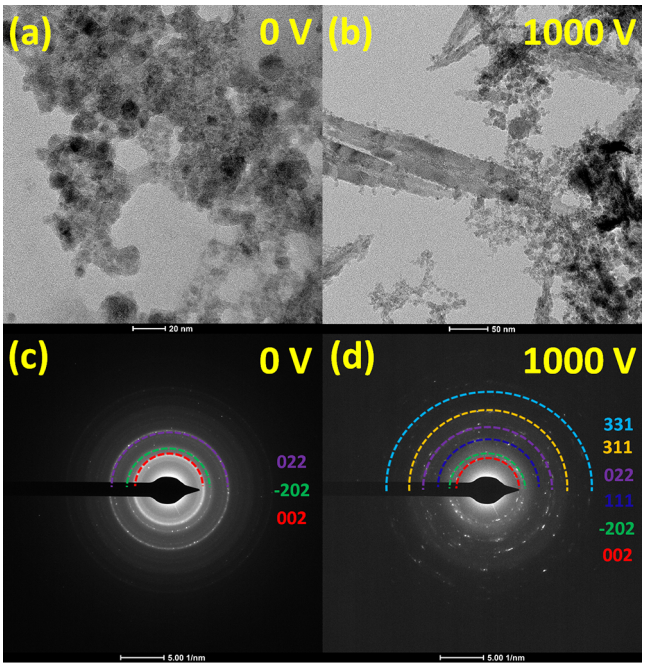

Figure 7. (a, b) TEM images of the Cu_xO NSs synthesized at 5.1 kHz under a potential difference of 0 and 1000 V, respectively. (c, d) Electron diffraction patterns corresponding to the TEM images shown in (a) and (b), respectively.

CuO NSs and around 3.2 eV for the Cu_2O NSs. Moreover, the electric field also helped enhance the concentration of the colloid by a factor of ∼5. Finally, this new synthesis protocol could be extended to synthesize other 3d transition-metal oxides, which will pave the path to new oxide heterostructure designs.

■ ASSOCIATED CONTENT

Supporting Information

The Supporting Information is available free of charge at https://pubs.acs.org/doi/10.1021/acsomega.1c05498.

Figure S1: pH versus the concentration of the Cu_xO NSs within the colloid; Figure S2: SEM images of the Cu_xO NSs synthesized by EFA-PLAL at 0 and 1000 V (PDF)

■ AUTHOR INFORMATION

Corresponding Author

Grégory Guisbiers − *Department of Physics & Astronomy, University of Arkansas at Little Rock, Little Rock, Arkansas 72204, United States;* orcid.org/0000-0002-4615-6014; Email: gxguisbiers@ualr.edu

Authors

Tina Hesabizadeh − *Department of Physics & Astronomy, University of Arkansas at Little Rock, Little Rock, Arkansas 72204, United States*

Nessrine Jebari − *Center of Nanosciences & Nanotechnologies, CNRS UMR 9001, University of Paris-Saclay, Paris 91120, France*

Ali Madouri − *Center of Nanosciences & Nanotechnologies, CNRS UMR 9001, University of Paris-Saclay, Paris 91120, France*

Géraldine Hallais − *Center of Nanosciences & Nanotechnologies, CNRS UMR 9001, University of Paris-Saclay, Paris 91120, France*

Trevor E. Clark − *Materials Characterization Lab, Pennsylvania State University, University Park, Pennsylvania 16802, United States*

Sanjay K. Behura − *Department of Chemistry and Physics, University of Arkansas at Pine Bluff, Pine Bluff, Arkansas 71601, United States;* orcid.org/0000-0001-7339-9997

Etienne Herth − *Center of Nanosciences & Nanotechnologies, CNRS UMR 9001, University of Paris-Saclay, Paris 91120, France*

Complete contact information is available at: https://pubs.acs.org/10.1021/acsomega.1c05498

Author Contributions

⊥T.H. and N.J. contributed equally to this work.

Notes

The authors declare no competing financial interest.

The data that support the findings of this study are available from the corresponding author upon reasonable request.

■ ACKNOWLEDGMENTS

The authors are grateful to the Center for Integrative Nanotechnology Sciences (CINS) of UA Little Rock for sharing their instruments (UV−visible−NIR and SEM). This work was partially supported by the French RENATECH network. S.K.B. acknowledges the MRFN Faculty Fellow Program 2021, which was supported by NSF through the Penn State University MRSEC DMR 1420620 & MRSEC DMR 2011839. T. H. and G. G. acknowledge UA Little Rock for its financial support.

■ REFERENCES

(1) Zhang, Q.; Zhang, K.; Xu, D.; Yang, G.; Huang, H.; Nie, F.; Liu, C.; Yang, S. CuO nanostructures: Synthesis, characterization, growth mechanisms, fundamental properties, and applications. *Prog. Mater. Sci.* **2014**, *60*, 208−337.

(2) Tokura, Y. Correlated-Electron Physics in Transition-Metal Oxides. *Phys. Today* **2003**, *56*, 50−55.

(3) Balık, M.; Bulut, V.; Erdogan, I. Y. Optical, structural and phase transition properties of Cu2O, CuO and Cu2O/CuO: Their photoelectrochemical sensor applications. *Int. J. Hydrogen Energy* **2019**, *44*, 18744−18755.

(4) Liang, Z.; Zhao, R.; Qiu, T.; Zou, R.; Xu, Q. Metal-organic framework-derived materials for electrochemical energy applications. *EnergyChem* **2019**, *1*, No. 100001.

(5) Jiang, B.; Wei, Y.; Wu, J.; Cheng, H.; Yuan, L.; Li, Z.; Xu, H.; Huang, Y. Recent progress of asymmetric solid-state electrolytes for lithium/sodium-metal batteries. *EnergyChem* **2021**, *3*, No. 100058.

(6) Steinhauer, S. Gas Sensors Based on Copper Oxide Nanomaterials: A Review. *Chemosensors* **2021**, *9*, 51.

(7) Yuan, G.; Yu, S.; Jie, J.; Wang, C.; Li, Q.; Pang, H. Cu/Cu2O nanostructures derived from copper oxalate as high performance electrocatalyst for glucose oxidation. *Chin. Chem. Lett.* **2020**, *31*, 1941−1945.

(8) Ye, W.; Guo, X.; Ma, T. A review on electrochemical synthesized copper-based catalysts for electrochemical reduction of CO2 to C2+ products. *Chem. Eng. J.* **2021**, *414*, No. 128825.

(9) Kim, S. J.; Kim, S.; Lee, J.; Jo, Y.; Seo, Y.-S.; Lee, M.; Lee, Y.; Cho, C. R.; Kim, J.-P.; Cheon, M.; Hwang, J.; Kim, Y. I.; Kim, Y.-H.; Kim, Y.-M.; Soon, A.; Choi, M.; Choi, W. S.; Jeong, S.-Y.; Lee, Y. H. Color of Copper/Copper Oxide. *Adv. Mater.* **2021**, *33*, No. 2007345.

(10) Wu, F.; Banerjee, S.; Li, H.; Myung, Y.; Banerjee, P. Indirect Phase Transformation of CuO to Cu_2O on a Nanowire Surface. *Langmuir* **2016**, *32*, 4485−4493.
(11) Yuan, M.; Guo, X.; Pang, H. Derivatives (Cu/CuO, Cu/Cu2O, and CuS) of Cu superstructures reduced by biomass reductants. *Mater. Today Chem.* **2021**, *21*, No. 100519.
(12) Tang, C.; Liao, X.; Zhong, W.; Yu, H.; Liu, Z. Electric field assisted growth and field emission properties of thermally oxidized CuO nanowires. *RSC Adv.* **2017**, *7*, 6439−6446.
(13) Hamdan, A.; Glad, X.; Cha, M. S. Synthesis of Copper and Copper Oxide Nanomaterials by Pulsed Electric Field in Water with Various Electrical Conductivities. *Nanomaterials* **2020**, *10*, 1347.
(14) Santillán, J. M. J.; Videla, F. A.; Fernandez van Raap, M. B.; Schinca, D. C.; Scaffardi, L. B. Analysis of the structure, configuration, and sizing of Cu and Cu oxide nanoparticles generated by fs laser ablation of solid target in liquids. *J. Appl. Phys.* **2013**, *113*, No. 134305.
(15) Ali, M.; Remalli, N.; Yehya, F.; Chaudhary, A. K.; Srikanth, V. V. S. S. Picosecond laser induced fragmentation of coarse Cu_2O particles into nanoparticles in liquid media. *Appl. Surf. Sci.* **2015**, *357*, 1601−1605.
(16) Roske, C. W.; Lefler, J. W.; Muller, A. M. Complex nanomineral formation utilizing kinetic control by PLAL. *J. Colloid Interface Sci.* **2017**, *489*, 68−75.
(17) Altuwirqi, R. M.; Albakri, A. S.; Al-Jawhari, H.; Ganash, E. A. Green synthesis of copper oxide nanoparticles by pulsed laser ablation in spinach leaves extract. *Optik* **2020**, *219*, No. 165280.
(18) Tiwari, P. K.; Shweta; Sing, A. K.; Singh, V. P.; Prasad, S. M.; Ramawat, N.; Tripathi, D. K.; Chauhan, D. K.; Rai, A. K. Liquid assisted pulsed laser ablation synthesized copper oxide nanoparticles (CuO-NPs) and their differential impact on rice seedlings. *Ecotoxicol. Environ. Saf.* **2019**, *176*, 321−329.
(19) Al-Jumaili, B. E. B.; Talib, Z. A.; Zakaria, A.; Ramizy, A.; Ahmed, N. M.; Paiman, S. B.; Ying, J. L.; Muhd, I. B.; Baqiah, H. Impact of ablation time on Cu oxide nanoparticle green synthesis via pulsed laser ablation in liquid media. *Appl. Phys. A: Mater. Sci. Process.* **2018**, *124*, No. 577.
(20) Gondal, M. A.; Qahtan, T. F.; Dastageer, M. A.; Saleh, T. A.; Maganda, Y. W.; Anjum, D. H. Effects of oxidizing medium on the composition, morphology and optical properties of copper oxide nanoparticles produced by pulsed laser ablation. *Appl. Surf. Sci.* **2013**, *286*, 149−155.
(21) Nath, A.; Das, A.; Rangan, L.; Khare, A. Bacterial Inhibition by Cu/Cu2O Nanocomposites Prepared via Laser Ablation in Liquids. *Sci. Adv. Mater.* **2012**, *4*, 106−109.
(22) Khashan, K. S.; Sulaiman, G. M.; Abdulameer, F. A. Synthesis and Antibacterial Activity of CuO Nanoparticles Suspension Induced by Laser Ablation in Liquid. *Arabian J. Sci. Eng.* **2016**, *41*, 301−310.
(23) Begildayeva, T.; Lee, S. J.; Yu, Y.; Park, J.; Kim, T. H.; Theerthagiri, J.; Ahn, A.; Jung, H. J.; Choi, M. Y. Production of copper nanoparticles exhibiting various morphologies via pulsed laser ablation in different solvents and their catalytic activity for reduction of toxic nitroaromatic compounds. *J. Hazard. Mater.* **2021**, *409*, No. 124412.
(24) Menazea, A. A.; Mostafa, A. M.; Al-Ashkar, E. A. Effect of nanostructured metal oxides (CdO, Al2O3, Cu2O) embedded in PVA via Nd:YAG pulsed laser ablation on their optical and structural properties. *J. Mol. Struct.* **2020**, *1203*, No. 127374.
(25) Rawat, R.; Tiwari, A.; Arun, N.; Rao, S. V. S. N.; Pathak, A. P.; Rao, S. V.; Tripathi, A. Synthesis of CuO hollow nanoparticles using laser ablation: effect of fluence and solvents. *Appl. Phys. A: Mater. Sci. Process.* **2020**, *126*, No. 226.
(26) Rajan, M. T.; Hassan, R.; Hong, H. P. Laser Plasma Induced Cu2O Nanoparticle Synthesis in Ethanol and Nanofluid Particle Characterization. *J. Nanofluids* **2019**, *8*, 1676−1682.
(27) Bhardwaj, A. K.; Kumar, V.; Pandey, V.; Naraian, R.; Gopal, R. Bacterial killing efficacy of synthesized rod shaped cuprous oxide nanoparticles using laser ablation technique. *SN Appl. Sci.* **2019**, *1*, No. 1426.
(28) Goncharova, D. A.; Kharlamova, T. S.; Lapin, I. N.; Svetlichnyi, V. A. Chemical and Morphological Evolution of Copper Nanoparticles Obtained by Pulsed Laser Ablation in Liquid. *J. Phys. Chem. C* **2019**, *123*, 21731−21742.
(29) Baruah, P. K.; Sharma, A. K.; Khare, A. Role of confining liquids on the properties of Cu@Cu2O nanoparticles synthesized by pulsed laser ablation and a correlative ablation study of the target surface. *RSC Adv.* **2019**, *9*, 15124−15139.
(30) Liu, P. S.; Li, Z. G.; Cai, W. P.; Fang, M.; Luo, X. D. Fabrication of cuprous oxide nanoparticles by laser ablation in PVP aqueous solution. *RSC Adv.* **2011**, *1*, 847−851.
(31) Tilaki, R. M.; Zad, A. I.; Mahdavi, S. M. Size, composition and optical properties of copper nanoparticles prepared by laser ablation in liquids. *Appl. Phys. A: Mater. Sci. Process.* **2007**, *88*, 415−419.
(32) Rafique, M.; Rafique, M. S.; Butt, S. H.; Afzal, A.; Kalsoom, U. Laser nature dependence on enhancement of optical and thermal properties of copper oxide nanofluids. *Appl. Surf. Sci.* **2019**, *483*, 187−193.
(33) Svetlichnyi, V. A.; Goncharova, D. A.; Shabalina, A. V.; Lapin, I. N.; Nemoykina, A. L. Cu2O Water Dispersions and Nano-Cu2O/Fabric Composite: Preparation by Pulsed Laser Ablation, Characterization and Antibacterial Properties. *Nano Hybrids Compos.* **2017**, *13*, 75−81.
(34) Azadi, H.; Aghdam, H. D.; Malekfar, R.; Bellah, S. M. Effects of energy and hydrogen peroxide concentration on structural and optical properties of CuO nanosheets prepared by pulsed laser ablation. *Results Phys.* **2019**, *15*, No. 102610.
(35) Tyurnina, A. E.; Shur, V. Y.; Kozin, R. V.; Kuznetsov, D. K.; Pryakhina, V. I.; Burban, G. V. Synthesis and investigation of stable copper nanoparticle colloids. *Phys. Solid State* **2014**, *56*, 1431−1437.
(36) Xiao, J.; Liu, P.; Wang, C. X.; Yang, G. W. External field-assisted laser ablation in liquid: An efficient strategy for nanocrystal synthesis and nanostructure assembly. *Prog. Mater. Sci.* **2017**, *87*, 140−220.
(37) https://www.rsc.org/periodic-table/element/29/copper.
(38) Guha, S.; Peebles, D.; Wieting, J. T. Raman and infrared studies of cupric oxide. *Bull. Mater. Sci.* **1991**, *14*, 539−543.
(39) Joya, M. R.; Barba-Ortega, J.; Raba, A. M. Vibrational Raman modes and particle size analysis of cupric oxide with calcination temperature. *Indian J. Pure Appl. Phys.* **2019**, *57*, 268−271.
(40) Xu, J. F.; Ji, W.; Shen, Z. X.; Li, W. S.; Tang, S. H.; Ye, X. R.; Jia, D. Z.; Xin, X. Q. Raman Spectra of CuO Nanocrystals. *J. Raman Spectrosc.* **1999**, *30*, 413−415.
(41) Debbichi, L.; Marco de Lucas, M. C.; Pierson, J. F.; Krüger, P. Vibrational Properties of CuO and Cu_4O_3 from First-Principles Calculations, and Raman and Infrared Spectroscopy. *J. Phys. Chem. C* **2012**, *116*, 10232−10237.
(42) Yu, P. Y.; Shen, Y. R. Multiple Resonance Effects on Raman Scattering at the Yellow-Exciton Series of Cu_2O. *Phys. Rev. Lett.* **1974**, *32*, 373−376.
(43) https://xpssimplified.com/elements/copper.php.
(44) Pauly, N.; Tougaard, S.; Yubero, F. Determination of the Cu 2p primary excitation spectra for Cu, Cu2O and CuO. *Surf. Sci.* **2014**, *620*, 17−22.
(45) Kuo, C. L.; Hwang, K. C. Does Morphology of a Metal Nanoparticle Play a Role in Ostwald Ripening Processes? *Chem. Mater.* **2013**, *25*, 365−371.
(46) Alloyeau, D.; Prévot, G.; Le Bouar, Y.; Oikawa, T.; Langlois, C.; Loiseau, A.; Ricolleau, C. Ostwald Ripening in Nanoalloys: When Thermodynamics Drives a Size-Dependent Particle Composition. *Phys. Rev. Lett.* **2010**, *105*, No. 255901.
(47) Dahonog, L. A.; Dela Vega, M. S. D. C.; Balela, M. D. L. pH-dependent synthesis of copper oxide phases by polyol method. *J. Phys.: Conf. Ser.* **2019**, *1191*, No. 012043.
(48) Zoolfakar, A. S.; Rani, R. A.; Morfa, A. J.; O'Mullane, A. P.; Kalantar-zadeh, K. Nanostructured copper oxide semiconductors: a perspective on materials, synthesis methods and applications. *J. Mater. Chem. C* **2014**, *2*, 5247−5270.

https://doi.org/10.1021/acsomega.1c05498
ACS Omega 2021, 6, 33130−33140

(49) Guisbiers, G. Advances in thermodynamic modelling of nanoparticles. *Adv. Phys. X* **2019**, *4*, No. 1668299.
(50) Geoffrion, L. D.; Guisbiers, G. Quantum confinement: Size on the grill! *J. Phys. Chem. Solids* **2020**, *140*, No. 109320.

https://doi.org/10.1021/acsomega.1c05498
ACS Omega 2021, 6, 33130−33140